SANDIA REPORT
SAND2009-5797
Unlimited Release
Printed September 2009

Nanostructures from Hydrogen Implantation of Metals

Markus D. Ong, Nancy Y. C. Yang, Ryan J. DePuit, Bruce R. McWatters, Rion A. Causey

Prepared by
Sandia National Laboratories
Albuquerque, New Mexico 87185 and Livermore, California 94550

Sandia is a multiprogram laboratory operated by Sandia Corporation,
a Lockheed Martin Company, for the United States Department of Energy's
National Nuclear Security Administration under Contract DE-AC04-94AL85000.

Approved for public release; further dissemination unlimited.

Sandia National Laboratories

Issued by Sandia National Laboratories, operated for the United States Department of Energy by Sandia Corporation.

NOTICE: This report was prepared as an account of work sponsored by an agency of the United States Government. Neither the United States Government, nor any agency thereof, nor any of their employees, nor any of their contractors, subcontractors, or their employees, make any warranty, express or implied, or assume any legal liability or responsibility for the accuracy, completeness, or usefulness of any information, apparatus, product, or process disclosed, or represent that its use would not infringe privately owned rights. Reference herein to any specific commercial product, process, or service by trade name, trademark, manufacturer, or otherwise, does not necessarily constitute or imply its endorsement, recommendation, or favoring by the United States Government, any agency thereof, or any of their contractors or subcontractors. The views and opinions expressed herein do not necessarily state or reflect those of the United States Government, any agency thereof, or any of their contractors.

Printed in the United States of America. This report has been reproduced directly from the best available copy.

Available to DOE and DOE contractors from
U.S. Department of Energy
Office of Scientific and Technical Information
P.O. Box 62
Oak Ridge, TN 37831

Telephone: (865) 576-8401
Facsimile: (865) 576-5728
E-Mail: reports@adonis.osti.gov
Online ordering: http://www.osti.gov/bridge

Available to the public from
U.S. Department of Commerce
National Technical Information Service
5285 Port Royal Rd.
Springfield, VA 22161

Telephone: (800) 553-6847
Facsimile: (703) 605-6900
E-Mail: orders@ntis.fedworld.gov
Online order: http://www.ntis.gov/help/ordermethods.asp?loc=7-4-0#online

SAND2009-5797
Unlimited Release
Printed September 2009

Nanostructures from Hydrogen Implantation of Metals

Markus D. Ong, Nancy Y. C. Yang, Ryan J. DePuit, Bruce R. McWatters, Rion A. Causey
Energy Nanomaterials Department

Bruce R. McWatters
Radiation-Solid Interactions Department

Sandia National Laboratories
P.O. Box 969
Livermore, California 94551-MS9291

Abstract

This study investigates a pathway to nanoporous structures created by hydrogen implantation in aluminum. Previous experiments for fusion applications have indicated that hydrogen and helium ion implantations are capable of producing bicontinuous nanoporous structures in a variety of metals. This study focuses specifically on hydrogen and helium implantations of aluminum, including complementary experimental results and computational modeling of this system. Experimental results show the evolution of the surface morphology as the hydrogen ion fluence increases from 10^{17} cm^{-2} to 10^{18} cm^{-2}. Implantations of helium at a fluence of 10^{18} cm^{-2} produce porosity on the order of 10 nm. Computational modeling demonstrates the formation of alanes, their desorption, and the resulting etching of aluminum surfaces that likely drives the nanostructures that form in the presence of hydrogen.

ACKNOWLEDGMENTS

The authors would like to acknowledge Jeffery Chames, Thomas Headley, and Michael Rye for their contributions to the electron microscopy characterization work and Norm Bartelt for his valuable insight with the computational effort. This work was performed under the Laboratory-Directed Research and Development program at Sandia National Laboratories, a multiprogram laboratory operated by Sandia Corporation, a Lockheed Martin Company, for the United States Department of Energy's National Nuclear Security Administration under contract DE-AC04-94-AL85000.

CONTENTS

1. Introduction 9

2. Background 11
   2.1. Implantations of Hydrogen 11
   2.2. Implantations of Helium 11
   2.3. Adsorption and Desorption of Hydrogen 12
   2.4. Al (111) Energy Landscape 12

3. Materials and Methods 15
   3.1. Experimental 15
      3.1.1. Material Preparation 15
      3.1.2. Material Characterization 16
   3.2. Computational Methods 16
      3.2.1. Background 16
      3.2.2. Algorithm and Implementation 17
      3.2.3. Lattice Gas Model 18

4. Experimental Results 21
   4.1. Optical and Scanning Electron Microscopy 21
   4.2. Cross-Section FIB and TEM 23
   4.3. Plan View TEM 28
   4.4. Helium Implantations 30

5. Computational Results 33
   5.1. Initial Conditions and Rate Laws 33
   5.2. Surface Equilibrium: Temperature and H Concentration Effects 34
   5.3. Desorption of Alanes and Step Etching 36

6. Conclusions and Future Work 39

7. References 42

FIGURES

Figure 3.1. Accelerator for ion implantations. 15

Figure 4.1. Optical micrograph of H implantation with a fluence of 3 x 10^{17} cm^{-2} (left) and 1 x 10^{18} cm^{-2} (right). 21

Figure 4.2. SEM micrographs of samples with (a) no hydrogen implantation, (b) hydrogen fluences of 1 x 10^{17} cm^{-2}, (c) 5 x 10^{17} cm^{-2}, and (d) 1 x 10^{18} cm^{-2}. Microscope conditions were 10 kV accelerating voltage, and 10,000x magnification. 22

Figure 4.3. SEM micrographs of H-implanted surfaces of Al with a fluence of 1 x 10^{18} cm^{-2}. Both images were taken at the same sample location, and the accelerating voltages used for the left and the right images were 4 kV and 10 kV, respectively. 23

Figure 4.4. FIB cross-sections of aluminum surfaces after hydrogen implantations with fluences of (a) 1 x 10^{17} cm^{-2}, (b) 5 x 10^{17} cm^{-2}, and (c) 1 x 10^{18} cm^{-2} 24

Figure 4.5. TEM cross-section montage for hydrogen fluence of 1 x 10^{17} cm^{-2} 25

Figure 4.6. TEM cross-section montage for hydrogen fluence of 5 x 10^{17} cm^{-2} 26

Figure 4.7. TEM cross-section montage for hydrogen fluence of 1 x 10^{18} cm^{-2} 27

Figure 4.8. TEM micrographs of two different tilt angles of the same cross-section area for a hydrogen fluence of 1 x 10^{18} cm^{-2} showing voids preferentially residing along grain boundaries. 28

Figure 4.9. Plan view TEM images for a sample implanted with a fluence of 1 x 10^{17} cm^{-2} showing (a) a representative view, (b) indications that a few voids begin to coalesce and (c) preferential void growth along grain boundaries. Lines marked "RD" in (a) and (b) indicate the rolling direction of the aluminum foil. 29

Figure 4.10. Plan view TEM images for a sample implanted with a fluence of 1 x 10^{18} cm^{-2} showing (a) preferential void coalescence along the rolling direction, (b) high magnification of void interconnectivity and (c) faceting indicating possible preferential etching along some surface orientations. 29

Figure 4.11. High Magnification SEM micrograph of He-implanted surface of Al. 30

Figure 4.12. Lower Magnification micrograph of He-implanted Al showing a smooth flake above the nanostructured surface. 31

Figure 5.1. Initial aluminum surface used in simulations. The white atoms represent the fixed subsurface aluminum that only provides the lattice sites for surface species. The black are adsorbed Al atoms, and are the only aluminum atoms that are free to diffuse and react. For clarity, only surface atoms will be shown in future illustrations. 33

Figure 5.2. Surface evolution at 100 K of (a) initial condition, 90% H coverage (b) using transition state theory kinetics (k_{ij}^{TST}) after 500,000 simulation time steps and (c) using a Metropolis-type potential energy-based kinetics ($k_{ij}^{\Delta E}$) after 20,000 time steps. Species legend: Al (gray), AlH (red), AlH2 (green), AlH3 (blue), adsorbed H (purple). Due to the orders of magnitude difference in diffusion and reaction rates, the transition state model based on activation energies requires an impractical number of time steps. As a result, the Metropolis-type potential energy based rate equation was used. 34

Figure 5.3. Effects of temperature and initial hydrogen coverage on distribution of surface species at equilibrium. The temperature produces only minor qualitative differences, whereas the hydrogen coverage is the limiting factor of the reaction of Al all the way to AlH_3. 35

Figure 5.4. Equilibrium state of the surface after reaction with adsorbed hydrogen at 100 K. No desorption was allowed, thus all hydrogen reacted with aluminum, forming AlH_3 (blue) and leaving only a few AlH (red) and AlH_2 (green) molecules remaining with original the aluminum adatoms (gray). Although the step edge has changed shape, using the simple lattice gas model, all species remain at step edges. 36

Figure 5.5. Surface after 15,000 time steps at 180 K to adsorb hydrogen onto the surface..... 36

Figure 5.6. Surface structure after placing adsorbed surface Figure 5.5 at 340 K for an additional 15,000 time steps, with desorption energy of AlH_3 specified to be 0.1 eV. The step width is noticeably smaller as AlH_3 has desorbed, effectively etching the step. 37

TABLES

Table 2.1. Elementary surface reaction energies from DFT calculations [13]. 13

Table 2.2. Selected binding energies for aluminum hydride species on Al (111). E_{bind} = *E(on surface) – E(cluster, vacuum) – E(Al surface)* [12]. Aluminum hydride binding energy is dependent on orientation, but is noticeably weaker than that of aluminum adatoms as well as adsorbed AlH. 13

Table 3.1. Index of implantation experiments 16

Table 4.1. EDS Elemental Composition for Hydrogen Implantations 23

Table 4.2. EDS Elemental Composition for Helium Implantations 31

NOMENCLATURE

Al	aluminum
AlH_3	alane
cm	centimeter
CVD	chemical vapor deposition\
DFT	density functional theory
DOE	Department of Energy
EDS	energy dispersive x-ray spectroscopy
eV	electron-Volt
FCC	face-centered cubic
FIB	focused ion beam
GPa	gigapascal
H	hydrogen
He	helium
K	Kelvin
keV	kilo electron-volt
KMC	kinetic Monte Carlo
kV	kilovolt
LG	lattice gas
MC	Monte Carlo
O	oxygen
ppm	parts per million
SEM	scanning electron microscopy
SNL	Sandia National Laboratories
TEM	transmission electron microscopy
TST	transition-state theory

1. INTRODUCTION

With many renewable energy sources of intermittent nature, energy storage will be important for the implementation of clean energy. This study investigates a pathway to nanoporous structures created by hydrogen implantation in metals. Nanoporous materials have high specific surface areas, making them ideal as supercapacitor electrodes. In experiments for fusion applications, formation of nanoporous films several micrometers thick was observed in tungsten surfaces exposed to helium plasma [1] and beryllium surfaces exposed to hydrogen [2]. Nanoscale features were produced near the irradiated surfaces, and the resulting porosity created bicontinuous structures. Other routes to formation of nanoporous metals such as dealloying or chemical reduction work well with noble metals, but cannot be used with electropositive metals such as aluminum or tungsten. This study focuses specifically on aluminum and the resulting morphology after implantation of hydrogen and helium ions. The formation and presence of volatile alanes contributes significantly to the resulting nanostructure when aluminum is implanted with hydrogen. The findings of complementary experimental and computational modeling of this system are included here in this report.

2. BACKGROUND

2.1. Implantations of Hydrogen

In the past few decades, many researchers have investigated the effects of energetic hydrogen implantation into metals, specifically as they relate to hydrogen recycling in the walls of fusion vessels [3, 4]. Recently, these studies have shifted to include the microstructural changes that result from ion implantation which play a crucial role in the development of a full understanding of the hydrogen recycling process.

When hydrogen is implanted into metals, it is believed that the hydrogen diffuses back to the surface and desorbs as molecular H_2 [4]. A steady state is reached when there is a balance between the implanted and recycled hydrogen [4]. However, within this process, hydrogen ions form bubbles due to their low solubility in many metals, including aluminum. These bubbles create concern because are reported to exhibit internal pressures of up to 7 GPa at room temperature [5], and play a key role in the mass transfer of hydrogen within the system.

As hydrogen fluence in aluminum is increased, instead of individual bubbles being formed, a tunnel structure is observed, characterized by a bicontinuous pore structure. This tunnel structure accommodates an increased hydrogen flux towards the surface. Furthermore, increased hydrogen fluence also leads to agglomeration of bubbles which may form blisters when they reach the surface. From experimental data it is evident that hydrogen concentration plays a critical role in the nature of the microstructure [4].

The interactions between hydrogen and aluminum surfaces themselves have been of particular interest, especially towards applications in the semiconductor industry [6, 7]. The surface interactions are very similar to those of implanted hydrogen, and it is therefore beneficial to study the surface behavior.

In addition to aluminum, there are numerous reports of hydrogen implantation in other metals demonstrating similar behavior [8]. Many different mechanisms have been proposed for void growth such as dislocation loop punching and vacancy clustering, but common findings are that voids tend to occur near the implantation depth and that low solubility of hydrogen in the metal gives rise to these structures [8].

2.2. Implantations of Helium

In addition to hydrogen, implantations of other elements have also produced similar nanostructures in metals. Wilson and Thomas reported blisters, flaking, and holes in aluminum at fluences of approximately 10^{17} cm^{-2} of helium ions [9]. The surface changes were dependent on fluence, flux, and temperature. More recently, Baldwin and Doerner produced similar nanoscale features forming on tungsten after bombardment of helium plasma [1]. The solubility of helium in these materials is expected to be negligible just as the solubility of hydrogen in the systems mentioned in the previous section, and this is appears to be one key to producing the voids and nanoscale features during ion implantation.

2.3. Adsorption and Desorption of Hydrogen

It is seen experimentally that when an aluminum surface is exposed to a flux of atomic hydrogen, aluminum hydride species (alanes) may be formed. Formation of alanes is negligible on the rough (100) and (110) surfaces, but quite significant on the smooth (111) surface. The formation of alanes has been shown to lead to hydrogen-induced etching of the surface [7].

Furthermore, on the Al (111) surface, up to 50% of the adsorbed hydrogen is found to desorb in the form of aluminum hydrides (alanes, or AlH_x). This desorption pathway exists in parallel to that of molecular hydrogen, and was found to reach a maximum rate near 340 K according to work by Hara, et al. [10]. However, in a separate study, Winkler et al. [11] found the formation and desorption of hydrides to be of minor significance at a heating rate of 3 K/s in comparison to the 10 K/s used by Hara et al., indicating the desorption of aluminum hydride also strongly depends on the heating rate used.

These reactions also have surface morphology consequences, as shown by Go et al. [7]. The surface alanes are more weakly bound to Al adatoms [12] and etch the smooth Al surface. However, the mechanistic details behind both the surface reactions and mass transfer are uncertain and only inferred from experimental observations. While the details are unknown, density functional theory (DFT) calculations show that AlH_2 and AlH_3 are more weakly bound than Al and AlH adatoms [12], which helps explain the surface morphology changes seen by Go et al.

2.4. Al (111) Energy Landscape

From the preceding section, it is clear that an understanding of the energy landscape of the surface is the foundation for any simulation. The detailed energy landscape may be computed on-the-fly from first principles using density functional theory (DFT). From the full landscape, it is trivial to calculate the potential energy of a state as well as any activation energy barriers for reactions. However, this is computationally demanding, so we take a different approach.

Instead of computing the full energy landscape on-the-fly, a finite number of reactions and their rates is tabulated a priori. When reaction pathways are present, the required energy only needs to be looked up from a pre-compiled rate catalog. In order for this to be valid, however, the catalog must contain all possible reaction pathways. To examine this we turn to the literature for the necessary thermodynamic energy calculations.

Due to their importance in the semiconductor industry for production of integrated circuits, there have been numerous studies into quantum chemical calculations of alane surface chemistry pertaining to aluminum chemical vapor deposition (CVD) from alane precursors [13]. Furthermore, alane clusters are a fundamental component of hydrogen storage materials, so we make use of the existing information regarding the thermodynamics of the elementary surface reactions in which we are interested.

Nakajima et al. used DFT and a cluster model to simulate deposition of aluminum from CVD of an alane precursor [13]. They calculated molecular structures, potential energies, and transition

states for the elementary reactions. The mechanism for aluminum deposition was determined to include the disassociation of AlH_3 into AlH_2, AlH, and H on the surface, followed by the cohesion of AlH, followed by the desorption of molecular hydrogen formed from this cohesion, leading to the deposition of aluminum in islands. The quantities relevant to our current investigation are summarized in Table 2.1. It is interesting to note that the proposed cohesion of AlH is not included in their calculations, so the corresponding energy diagram is unknown. However, we are interested in the inverse process of CVD, so this uncertainty is immaterial.

Table 2.1. Elementary surface reaction energies from DFT calculations [13].

	ΔE (eV)	E_a (eV)
Al(ad) + H(ad) → AlH(ad)	-0.806	0.000
AlH(ad) + H(ad) → AlH_2(ad)	-0.273	0.087
AlH_2(ad) + H(ad) → AlH_3(ad)	-0.009	0.191
H(ad) + H(ad) → H_2(g)	-0.668	0.130
AlH(ad) + H(ad) → Al(ad) + H_2(g)	0.369	0.863
AlH_2(ad) + H(ad) → AlH(ad) + H_2(g)	0.039	0.806
AlH_3(ad) + H(ad) → AlH_2(ad) + H_2(g)	-0.529	0.529

In another study, Chaudhuri et al. invested the formation and oligomerization of alane clusters from adsorbed hydrogen on the Al (111) surface using both experimental (surface IR) and theoretical techniques (DFT) [12]. They found that at high H coverages, step edges become favorable sites for adsorption of atomic hydrogen, and AlH_3 likely forms here at saturation. At higher concentrations of hydrogen, they propose that AlH_3 is extracted from the step edge and becomes weakly bound and highly mobile on the flat surface. It is this process that accounts for the step etching observed in other experimental studies.

Table 2.2. Selected binding energies for aluminum hydride species on Al (111). E_{bind} = *E(on surface) – E(cluster, vacuum) – E(Al surface)* [12]. Aluminum hydride binding energy is dependent on orientation, but is noticeably weaker than that of aluminum adatoms as well as adsorbed AlH.

Environment	Binding energy (eV)
Adatom or Al-H	-3.54
H (step)	-3.90
H (terrace)	-3.05
AlH_3 (step)	-0.99
AlH_3 (terrace,semihorizontal)	-3.87
AlH_3 (terrace,vertical)	-0.91

3. MATERIALS AND METHODS

3.1. Experimental

3.1.1. Material Preparation

High purity, as-rolled aluminum foil produced by Goodfellow was used for the implantation experiments. Purity was quoted as 99.999% with no element other than oxygen occurring in traces greater than 5 ppm. The thickness of the foils was 0.050 mm, and each piece was 25 mm square. Marks indicating the rolling direction could be easily observed, particularly at high magnifications.

Ion implantations were done using a Cockroft Walton accelerator shown in Figure 3.1 capable of implanting singly charged ions at energies from 25 to 250 keV. The implantations used in this study were low-energy implantations at 25 keV. A mask was used to expose only the center 10 mm square of the aluminum foil to the ion beam in order to ensure an even distribution of the fluence over the entire implant region with the beam raster. High purity hydrogen and helium in compressed gas cylinders were connected to the accelerator depending on which source was required for each implant. All implantations were done at room temperature, and fluences were progressively varied from 1×10^{17} cm^{-2} to 1×10^{18} cm^{-2}. An index of implantation experiments are shown in Table 3.1.

Figure 3.1. Accelerator for ion implantations.

Table 3.1. Index of implantation experiments

Index	Implant Ion	Fluence
01	None	None
02	Hydrogen	1×10^{17} cm^{-2}
03	Hydrogen	3×10^{17} cm^{-2}
04	Hydrogen	5×10^{17} cm^{-2}
05	Hydrogen	1×10^{18} cm^{-2}
06	Helium	1×10^{18} cm^{-2}

3.1.2. Material Characterization

Material characterization was accomplished using a variety of optical and electron microscopy techniques. Initial images were captured using a digital camera, a scanner, and a Leitz optical microscope. Scanning electron microscopy (SEM) was done with a JEOL 6400 field emission microscope, including elemental analysis by energy dispersive x-ray spectroscopy (EDS). Subsequent characterization used a focused ion beam (FIB) to sputter away material to reveal a cross-section of the post-implanted sample. In addition to the scanning secondary electron microscopy of the cross-section, the FIB also produced a transmission electron microscopy (TEM) sample of the exact same slice of material. Complementary plan view TEM was also performed using samples that were electrochemically thinned starting from the back surface opposite the surface facing the ion implantation beam and leaving only approximately 200 nm of the implanted surface.

3.2. Computational Methods

3.2.1. Background

Monte Carlo (MC) simulations use random numbers to solve problems, and got its name from the random nature of gambling in Monte Carlo, Monaco. The most well-known algorithm is the Metropolis Monte Carlo algorithm, invented in the 1950s at Los Alamos National Laboratories. Since its original inception, additional MC algorithms have been developed to improve computational time, as well as to incorporate the dynamical evolution between states. One such algorithm is the dynamic or kinetic Monte Carlo (KMC) algorithm.

Kinetic Monte Carlo was born out of the time-scale limitations of the traditional molecular dynamics framework for atomistic simulations, which evolve a system according to the classical equations of motion. This straightforward process relies on understanding the interactions between atoms, computing the forces, and evolving the system accordingly. However, this technique is limited to very small time-steps required to resolve atomic vibrations which occur on the scale of 10^{-15} s. Consequently, the total simulation time only reaches of order nanoseconds for 10^{6} steps. Kinetic Monte Carlo techniques offer a solution to this by coarse-graining the definition of a state and looking at diffusive jumps between states rather than minor individual atomic vibrations within each state.

Additionally, in traditional Metropolis Monte Carlo, trial moves are selected at random, and often rejected at low temperatures or near equilibrium when most moves are no longer energetically favorable, where KMC typically uses a rejection-free algorithm. However, KMC requires that the possible states be finite so reaction pathways can be specified, whereas MC allows for infinite states, including unknown states, making it more useful for large configuration spaces such as a system which models protein folding.

3.2.2. Algorithm and Implementation

The procedure for the stochastic algorithm is straightforward, assuming the rate constants are either known or may be calculated for all possible pathways. Consider a system in its current state i, from which we have knowledge of all the pathways j and corresponding rate constants k_{ij}. Each pathway has a characteristic probability distribution of first-escape times t, given by

$$p_{ij}(t) = k_{ij}\exp(-k_{ij}t)$$

Since the system may only evolve according to one of these pathways, it is allowed to evolve by whichever pathway has the shortest first-escape. To do this, an exponentially distributed random time t_j is selected from each pathway j, and the pathway corresponding to the minimal time t_j is chosen. The system is then moved to the new state $j_{\min}$, and the simulation clock is advanced by t_j.

Although the above procedure illustrates the algorithm, it is not the most computationally efficient to implement, and our simulations used a more efficient implementation of KMC. First, we created list of all possible events and their rate constants. The transition-state theory (TST) rate laws k_{ij}^{TST} may be calculated from a known activation energy E_a

$$k_{ij}^{TST} = A\exp(-E_a / k_B T)$$

where k_B is the Boltzmann constant and T is the temperature. Next, an array of partial sums $S(j)$ of the rates is taken to get a total length k_{tot} for the pathways vector.

$$S(j) = \sum_{m}^{j} k_{im}$$

A position along this array is selected from a random number *rand* uniformly distributed on (0,1) and multiplied by k_{tot}.

$$k_{tot} = \sum_{j} k_{ij}$$

The pathway is selected by stepping through the array until $S(p) > rand\ k_{tot}$, which selects pathway p and the system is evolved accordingly. Finally, a second random number, r, is selected from an exponential distribution for k_{tot} given by

$$t_{clock} = -(1/k_{tot})\ln(r)$$

The simulation clock is advanced by t_{clock}, and this process is repeated. Here, the time stepping is independent of the actual pathway chosen, and depends only on the sum of the rates [14].

However, that there are orders or magnitude difference in time scales for diffusion rates and reaction rates from TST. Due to the low energy barriers on the Al (111) surface, adatoms diffuse approximately three orders of magnitude faster than they react. As a result, the simulation requires an extremely large number of time steps to accurately capture both of these behaviors. As a result, we can examine only equilibrium structures and calculate rates based on changes in potential energy according to

$$k_{ij}^{\Delta E} = A\frac{\exp(-\Delta E/2k_BT)}{\exp(-\Delta E/2k_BT)+\exp(+\Delta E/2k_BT)}$$

which is chosen to automatically satisfy reversibility and detailed balance [15]. Although the true kinetic dynamical evolution is lost, the simulations require much less time (20,000 time steps, as compared to > 1,000,000 steps), allowing proper equilibrium to be reached. While this is effectively the Metropolis criterion, the incorporation of the kinetic MC approach drastically improves computation time.

3.2.3. Lattice Gas Model

We modeled the surface system with the simplest of models: a two-dimensional lattice gas (LG). Here, all atoms and molecules are approximated by a single sphere with a radius equal to the Al atomic radius. Furthermore, the spheres were restricted to only the fixed face-centered cubic (FCC) lattice sites of the Al (111) surface.

In this model, the energy is approximated by a Lattice Gas Hamiltonian *H*:

$$H = E_{ad}\Sigma_i n_i + V_{ij}\Sigma_{ij} n_i n_j$$

where E_{ad} is the energy of an individual adatom, *n* is 1 for occupied sites and 0 for vacant sites, and V_{ij} is the interaction energy between adatoms. The first term on the right side represents the total energy of the adsorbed species, thus the sum is taken over all lattice sites. The second term represents the energy arising from interactions between the adsorbed species, which in the LG model are limited to only interactions between nearest neighbors. In other words, the summation in the second term represents the number of nearest neighbors.

From the literature for Al, we make a general approximation that these energies may be assumed to be equal for all species, and take $E_{ad} = 1.05\,eV$ [16] and approximate $V_{ij} = -0.35\,eV$. This value for the interaction energy was arrived from activation energy data for Al self-diffusion, and an assumed linear relationship with the number of nearest neighbors

$$E_a = E_{a,0}\left(1 - V_{ij}\Sigma_{ij} n_i n_j\right)$$

where $E_{a,0} = 0.04\,eV$, and $E_a = -0.8\,eV$ for diffusion away from a step when an adatom has 2 or more nearest neighbors. Substitution of these values into the above expression yields a value for V_{ij} of approximately -0.35 eV. Although system kinetics are typically based on transition-state theory and activation energies, here they are based on thermodynamic potential energies taken from the literature in this problem.

4. EXPERIMENTAL RESULTS

4.1. Optical and Scanning Electron Microscopy

After hydrogen implantation, the bombarded regions turn a dark yellow, nearly brown color at high fluences. At lower doses, the color is a fainter yellow. This is shown in Figure 4.1 with the image of a lower dose foil on the left having a fainter square and the image of a high dose foil on the right having a darker square. This is likely due to the accumulation of surface oxides and carbon during the ion implantation. Also, the surface in the implanted region is rougher due to the small morphological changes. While these features cannot be directly observed with an optical image using visible light, the additional scattering due to the nanoscale roughness should make the surface appear darker.

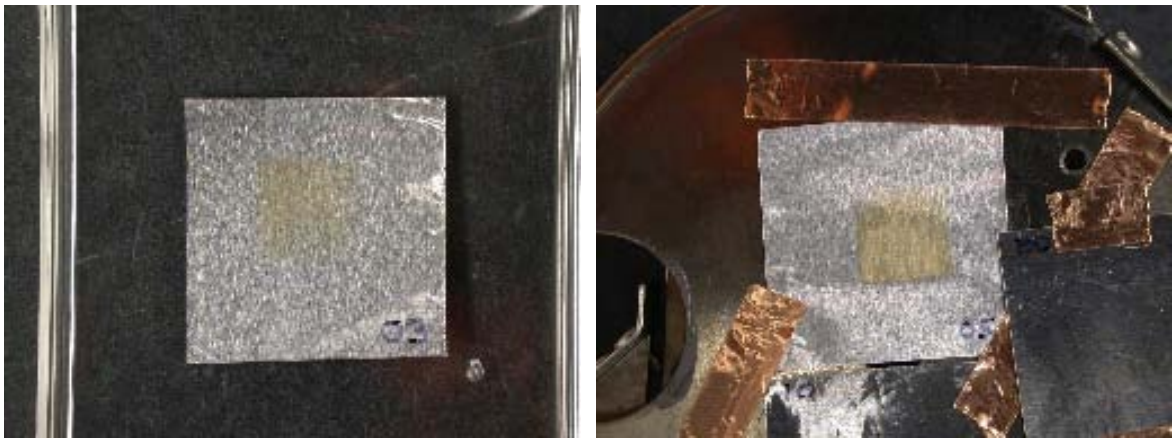

Figure 4.1. Optical micrograph of H implantation with a fluence of 3 x 10^{17} cm^{-2} (left) and 1 x 10^{18} cm^{-2} (right).

SEM micrographs show more detail of the surface structure of the samples and reinforce the roughness indications of the optical images. The images shown in Figure 4.2 show the progressive development of the porous structure as the implant dose goes from the initial, pre-implanted, state to the a final dose of 1 x 10^{18} cm^{-2}. Surface grinding marks are visible for the as-rolled foil, but there is no evidence of porosity in this initial state. The formation of bubbles is already evident, however, even at the lowest fluence. The intermediate step of 5 x 10^{17} cm^{-2} shows that the porosity has formed throughout the structure, and at the highest fluence of 1 x 10^{18} cm^{-2}, the porosity is beginning to coalesce into large blisters.

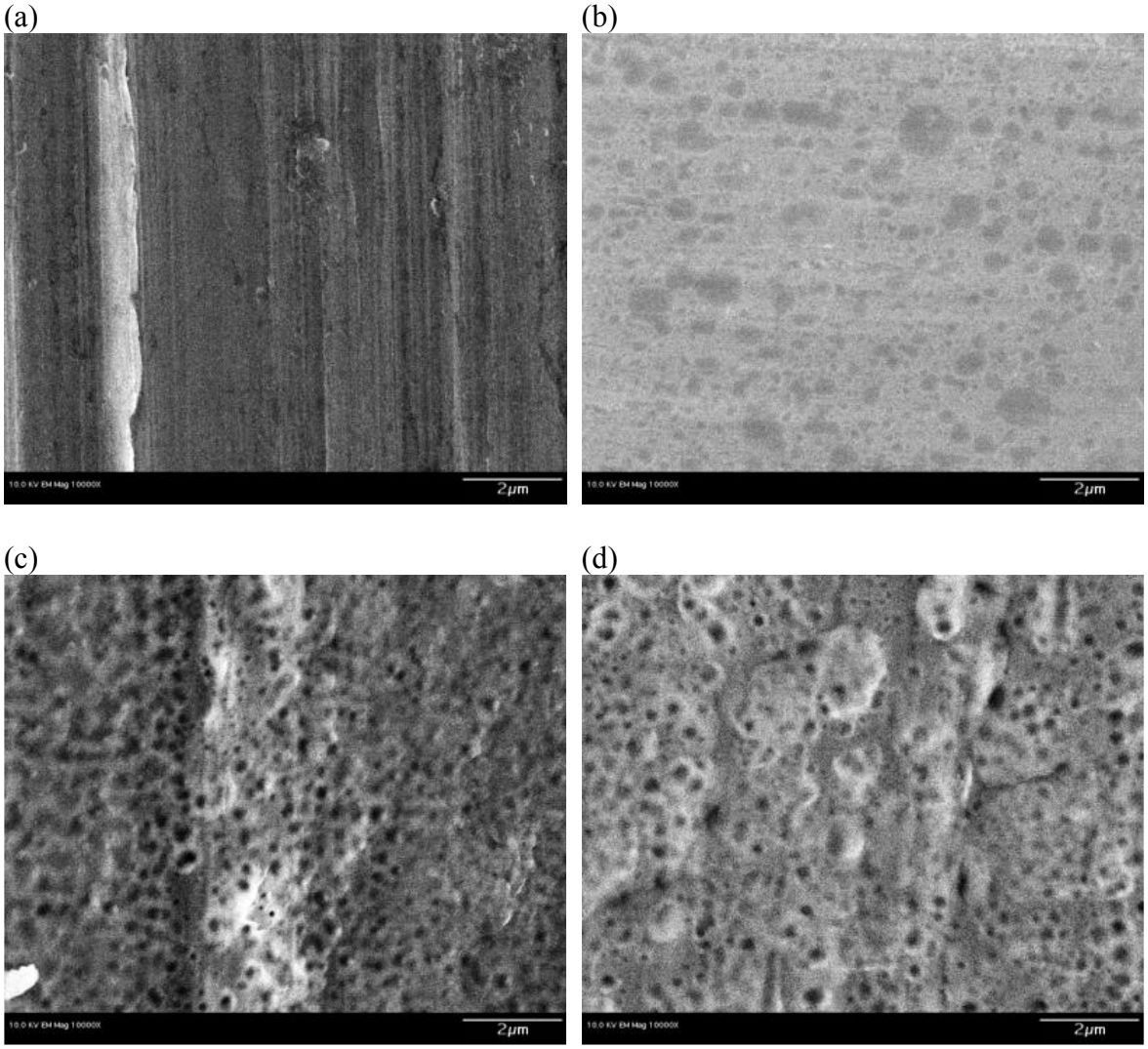

Figure 4.2. SEM micrographs of samples with (a) no hydrogen implantation, (b) hydrogen fluences of 1 x 10^{17} cm^{-2}, (c) 5 x 10^{17} cm^{-2}, and (d) 1 x 10^{18} cm^{-2}. Microscope conditions were 10 kV accelerating voltage, and 10,000x magnification.

Varying the accelerating voltage used in SEM imaging gives additional scientific information about the sample because the excitation volume likewise varies. This is evident in Figure 4.3 which shows the 1 x 10^{18} cm^{-2} implantation using two different imaging conditions. The image on the left is taken with an accelerating voltage of 4 kV, and only surface blisters can be observed. Because the excitation volume is small, no subsurface porosity can be detected. However, the image on the right, taken at 10 kV, is able to image the porosity beneath a thin skin of material seen in the 4 kV images. The two microscope conditions are complementary and, when taken together, give a more complete understanding of the morphological changes near the surface. Similar results are seen with a fluence of 5 x 10^{17} cm^{-2}, but not for a fluence of 1 x 10^{17} cm^{-2}.

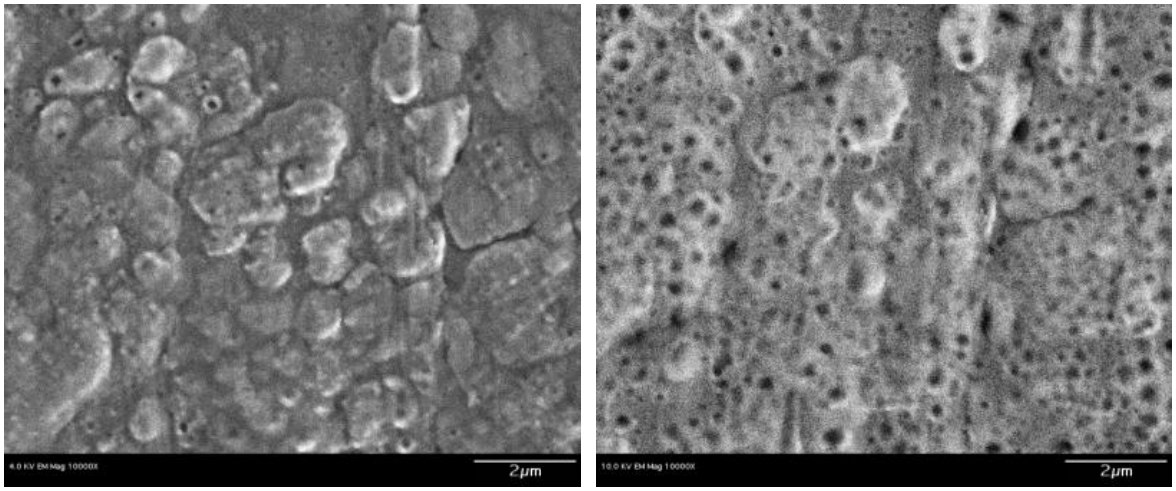

Figure 4.3. SEM micrographs of H-implanted surfaces of Al with a fluence of 1 x 10^{18} cm^{-2}. Both images were taken at the same sample location, and the accelerating voltages used for the left and the right images were 4 kV and 10 kV, respectively.

The original plan to quantify surface area using either electrochemistry and/or porosimetry did not work out due to the small amount of sample produced during this short project. However, information about the surface area can be deduced from analytical SEM techniques. EDS was used to quantify the oxygen in certain areas of the foils. Higher amounts oxygen was indicative of additional aluminum oxide that grows readily on newly formed aluminum surfaces. Therefore, the amount of oxygen can be considered a reasonable proxy for surface area measurements. The EDS results in Table 4.1 show that the lowest fluence results in a higher oxygen content, hence a higher surface area, than regions without any implantations. Moving to higher doses increases the oxygen and corresponding surface area further. This result is consistent with the SEM images showing additional porosity generated at higher doses.

Table 4.1. EDS Elemental Composition for Hydrogen Implantations

Fluence	O/Al Ratio (by at %)
None	0.018
1 x 10^{17} cm^{-2}	0.021
5 x 10^{17} cm^{-2}	0.025
1 x 10^{18} cm^{-2}	0.026

4.2. Cross-Section FIB and TEM

Cross-section images were taken after using a FIB to sputter away material and are shown in Figure 4.4. These data are in good qualitative agreement with the SEM images and show very few voids for the lowest dose and increasingly more voids as the implantation fluence increases. Note that the brighter region above the aluminum surface is platinum that was deposited over the aluminum surface to stabilize it as the FIB removed material to reveal the cross-section. TEM cross-section samples were also prepared along the same plane shown in the FIB images. These are shown in Figure 4.5, Figure 4.6, and Figure 4.7 as montages of a set of neighboring sections

for each of the three fluences. Tilting the TEM sample holder to orient the sample to optimize contrast between the grains shows that the voids, particularly larger ones, are preferentially located along grain boundaries and other microstructural defects in the aluminum. These images are shown in Figure 4.8.

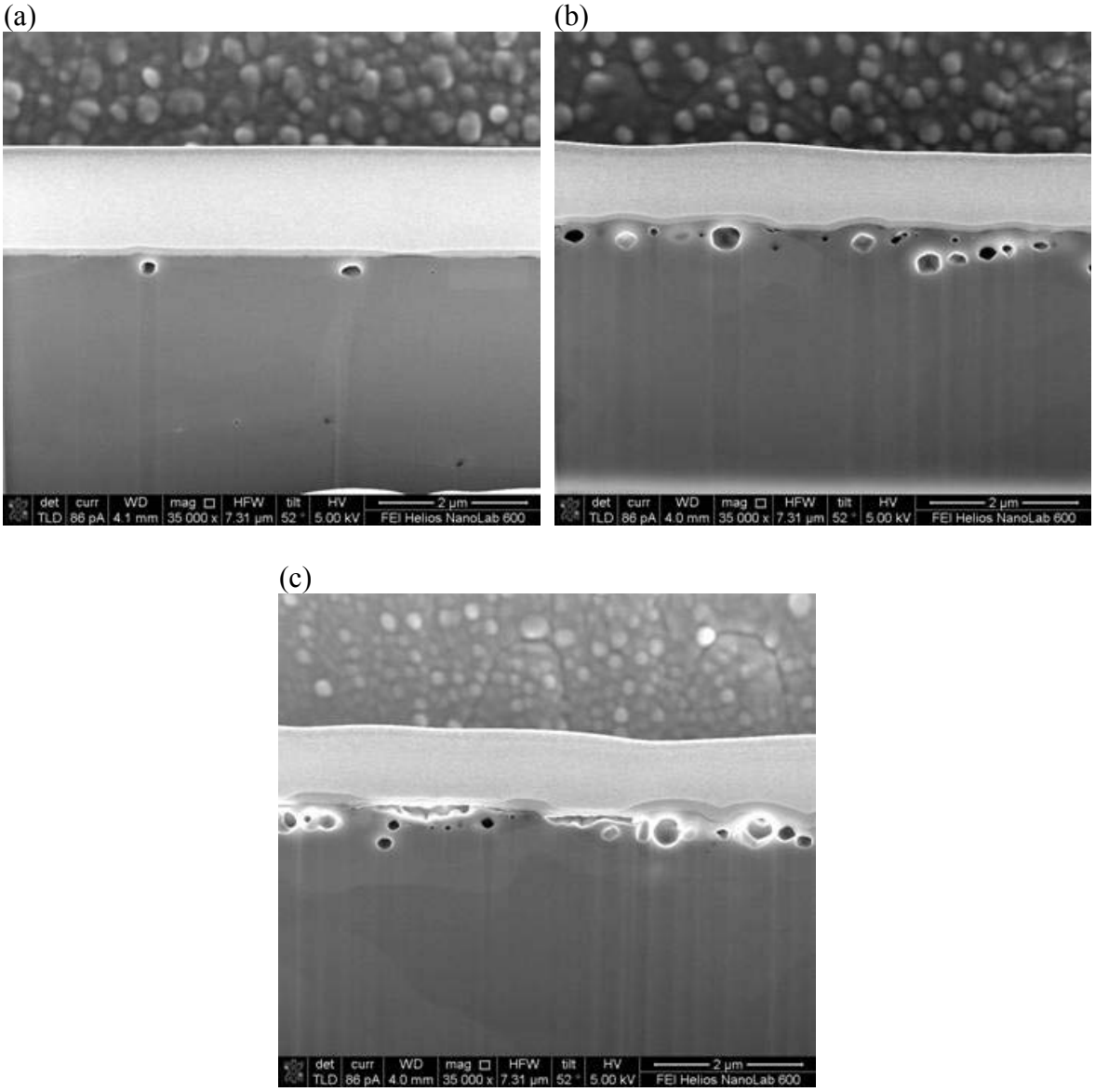

Figure 4.4. FIB cross-sections of aluminum surfaces after hydrogen implantations with fluences of (a) 1 x 10^{17} cm^{-2}, (b) 5 x 10^{17} cm^{-2}, and (c) 1 x 10^{18} cm^{-2}.

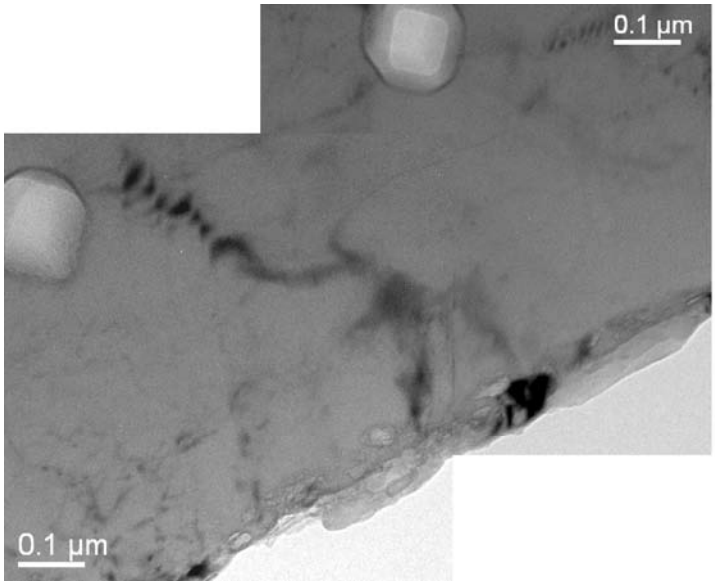

Figure 4.5. TEM cross-section montage for hydrogen fluence of 1 x 10^{17} cm^{-2}.

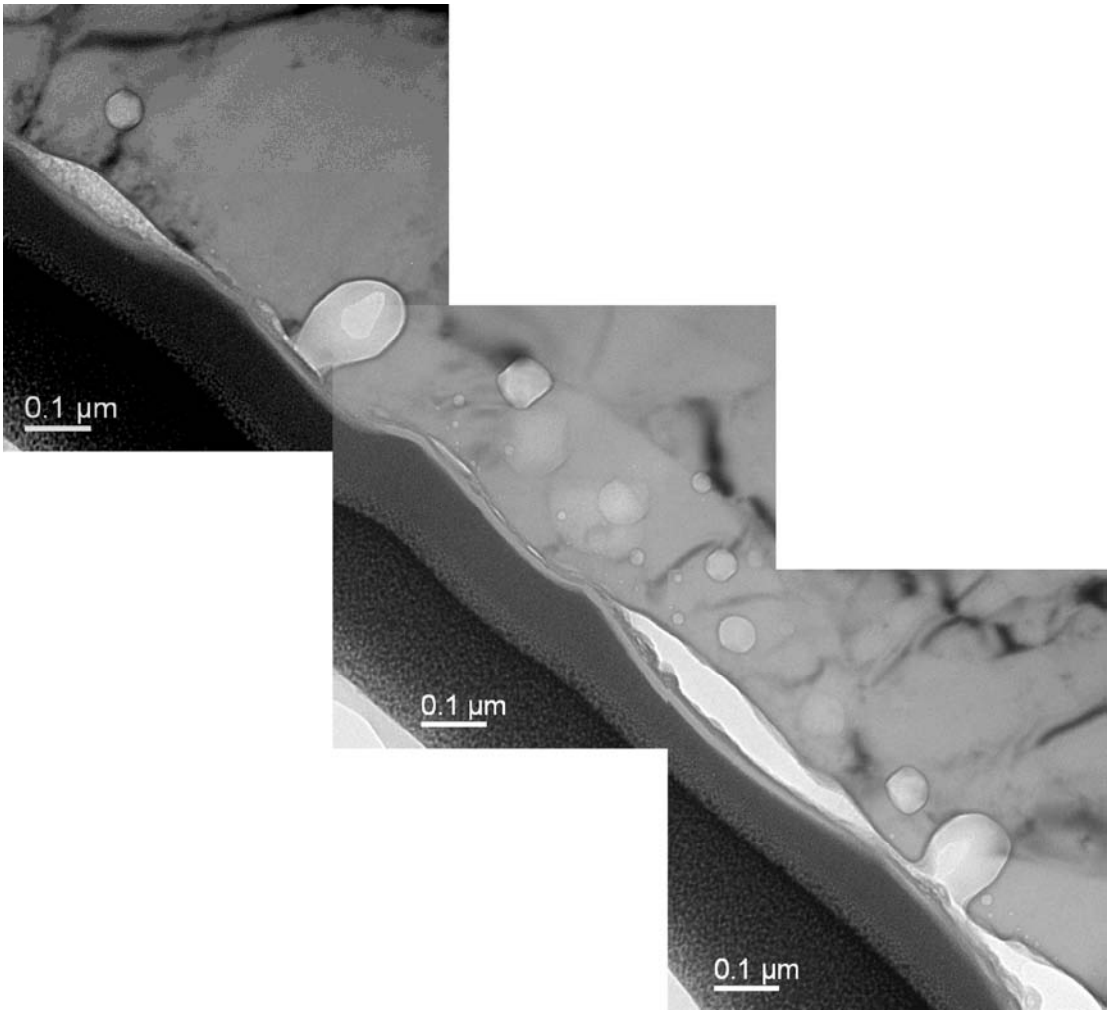

Figure 4.6. TEM cross-section montage for hydrogen fluence of 5 x 10^{17} cm^{-2}.

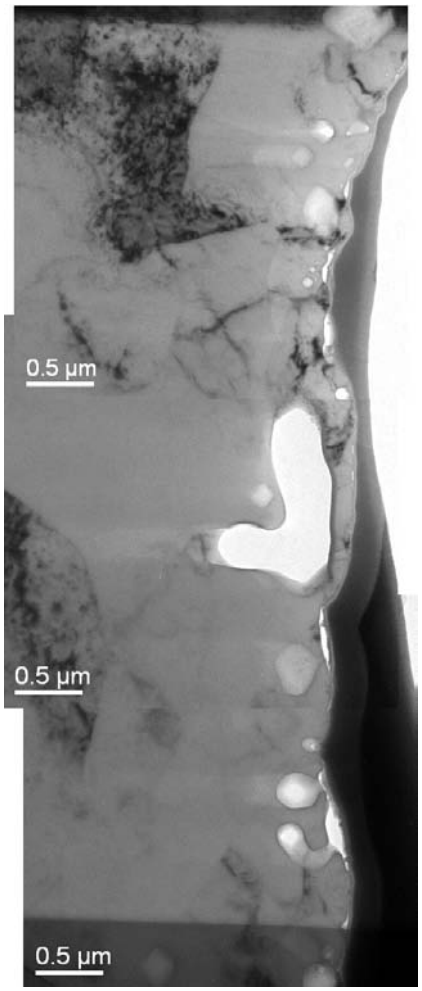

Figure 4.7. TEM cross-section montage for hydrogen fluence of 1 x 10^{18} cm^{-2}.

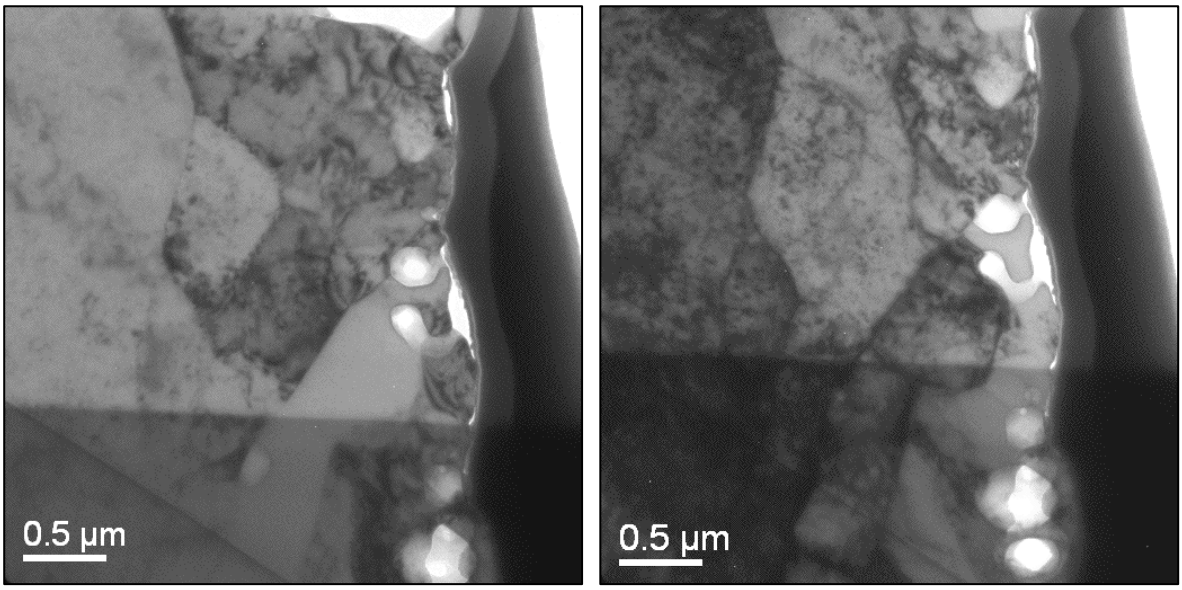

Figure 4.8. TEM micrographs of two different tilt angles of the same cross-section area for a hydrogen fluence of 1 x 10^{18} cm^{-2} showing voids preferentially residing along grain boundaries.

4.3. Plan View TEM

Although voids may not appear to be intersecting in an image from a cross-section sample, it is possible that they may intersect at a point slightly removed from the sampling plane. Plan view TEM gives additional insight to the porous structure at the top 200 nm of the surface because it can sample a relatively large surface area and thus more voids compared to the cross-section techniques. Plan view images from a sample implanted with a fluence of 1 x 10^{17} cm^{-2} are shown in Figure 4.9. These images show that most of the voids are relatively small and few have coalesced into larger voids. The porous structure is not bicontinuous, and the pores tend to align themselves with the rolling direction. Void growth appears to be preferential along grain boundaries when they are in the vicinity.

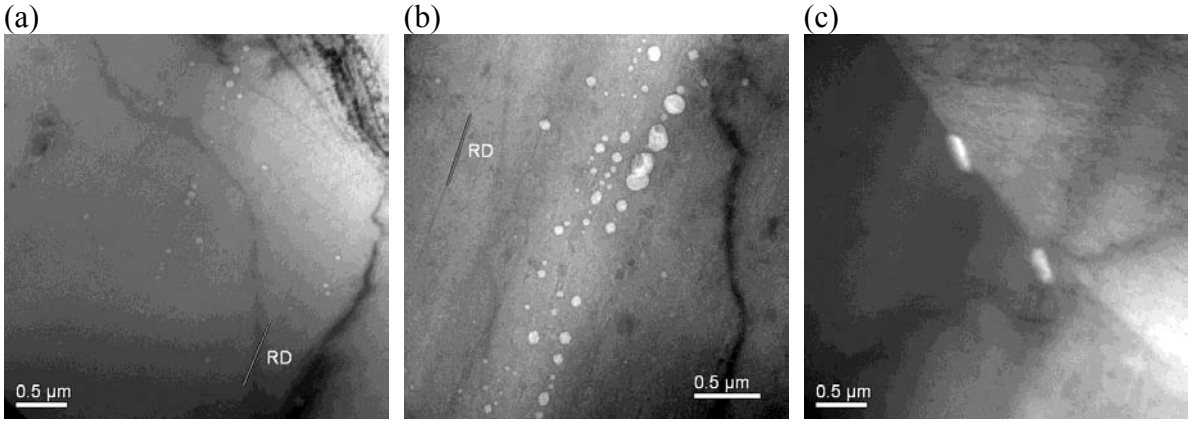

Figure 4.9. Plan view TEM images for a sample implanted with a fluence of 1 x 10^{17} cm^{-2} showing (a) a representative view, (b) indications that a few voids begin to coalesce and (c) preferential void growth along grain boundaries. Lines marked "RD" in (a) and (b) indicate the rolling direction of the aluminum foil.

At a fluence of 1 x 10^{18} cm^{-2}, an order of magnitude higher, there are many more voids, and the voids appear to be much more interconnected. The plan view TEM images are shown in Figure 4.10. The images in Figure 4.9 showed that voids clustered along the rolling direction, and it is not surprising to find that void coalescence likewise occurs in the same fashion. For the lower fluence sample, only a few of the voids were interconnected, but for this higher fluence sample, it appears that many of the voids are interconnected. It is also interesting to note that some of the voids appear to be faceted as if some surfaces are preferentially etching along crystallographic planes of the aluminum. This is particularly interesting when considered in conjunction with the fact that volatile alanes preferentially form along the Al (111) surface as discussed in Section 2.3.

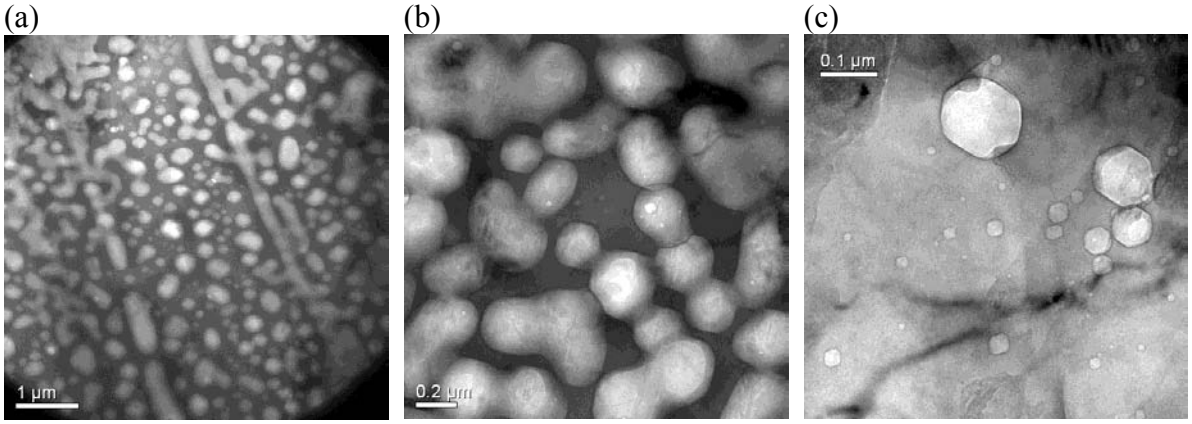

Figure 4.10. Plan view TEM images for a sample implanted with a fluence of 1 x 10^{18} cm^{-2} showing (a) preferential void coalescence along the rolling direction, (b) high magnification of void interconnectivity and (c) faceting indicating possible preferential etching along some surface orientations.

4.4. Helium Implantations

Helium implantations were done in the same manner as the hydrogen implantations in order to determine the relative importance of the hydrogen chemistry with aluminum. Both helium and hydrogen are virtually insoluble in aluminum, but helium is inert and will not form alanes or other aluminum hydride species that can desorb and restructure the aluminum surface. A high resolution SEM micrograph of the structure resulting from an implant fluence of 1 x 10^{18} cm^{-2} He ions is shown in Figure 4.11. Small scale porosity on the order of 10 nm is formed from the helium implantations. Lower magnification micrographs such as the one in Figure 4.12 show smooth flakes above the porous surface in some regions. It is likely that the exposed porous structures are revealed only in areas where these skin layers have flaked off [9]. The EDS of the helium implanted samples also indicates a higher surface area than the hydrogen samples implanted with the same fluence as shown in Table 4.2.

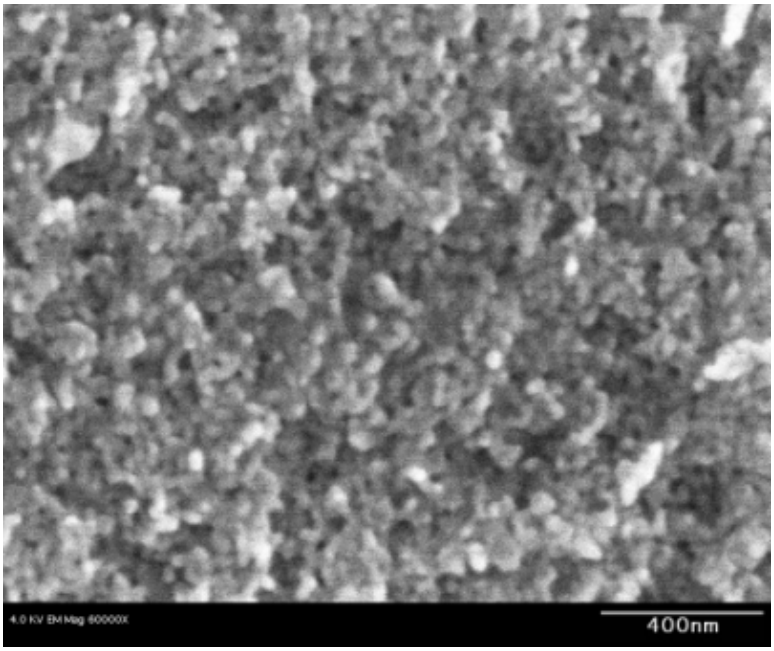

Figure 4.11. High Magnification SEM micrograph of He-implanted surface of Al.

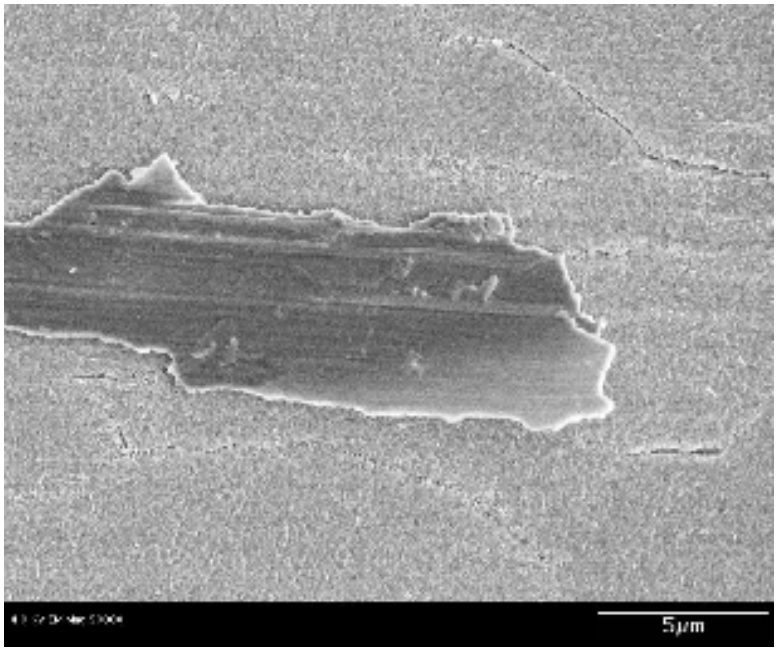

Figure 4.12. Lower Magnification micrograph of He-implanted Al showing a smooth flake above the nanostructured surface.

Table 4.2. EDS Elemental Composition for Helium Implantations

Fluence	O/Al Ratio (by at %)
None	0.017
1×10^{18} cm^{-2}	0.035

5. COMPUTATIONAL RESULTS

5.1. Initial Conditions and Rate Laws

It is evident from the literature that surface morphology plays a crucial role in the development of a microstructure. As such, we consider an aluminum surface that includes a step, illustrated in Figure 5.1, and is also periodic in both directions. Atoms are restricted to FCC lattice sites of the Al (111) surface and interact with only the 6 nearest neighbors. Simulations are kept to a small domain of 15 x 15 that can be run on a desktop computer and provide a qualitative understanding of the surface evolution.

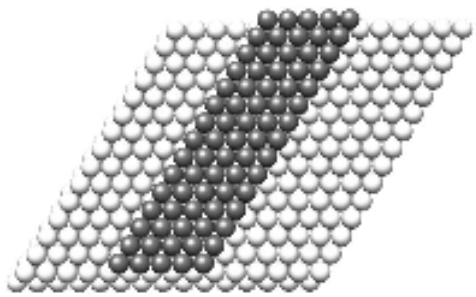

Figure 5.1. Initial aluminum surface used in simulations. The white atoms represent the fixed subsurface aluminum that only provides the lattice sites for surface species. The black are adsorbed Al atoms, and are the only aluminum atoms that are free to diffuse and react. For clarity, only surface atoms will be shown in future illustrations.

The surface structure evolution is broken down into two stages. First, the surface equilibrium and the reactions of adsorbed hydrogen with the aluminum surface are examined. Next, the desorption process and its properties are investigated in order to reproduce experimental structures showing H-induced step etching [7].

First, we comment on the nature of the rate law. Section 3.2.2 alluded to the fact that there are different time scales present, which makes the use of TST rate laws impractical. Figure 5.2 compares the results of two simulations, both with an initial H coverage of 90%. The use of transition state theory does not result in an equilibrium state, so the kinetic model is restricted to potential energies in order to obtain equilibrium results. Consequently, the true dynamical evolution of the surface is not captured and the analysis is constrained to equilibrium states

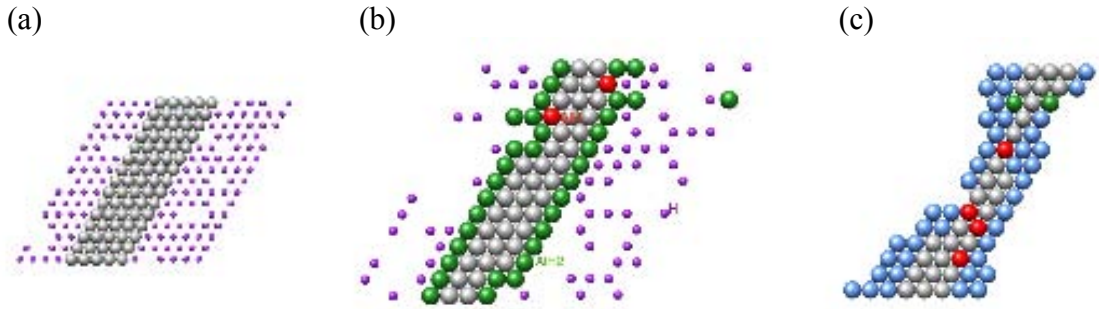

Figure 5.2. Surface evolution at 100 K of (a) initial condition, 90% H coverage (b) using transition state theory kinetics (k_{ij}^{TST}) after 500,000 simulation time steps and (c) using a Metropolis-type potential energy-based kinetics ($k_{ij}^{\Delta E}$) after 20,000 time steps. Species legend: Al (gray), AlH (red), AlH2 (green), AlH3 (blue), adsorbed H (purple). Due to the orders of magnitude difference in diffusion and reaction rates, the transition state model based on activation energies requires an impractical number of time steps. As a result, the Metropolis-type potential energy based rate equation was used.

5.2. Surface Equilibrium: Temperature and H Concentration Effects

The first stage in the simulation examined the equilibrium state of the surface, specifically focusing on the distribution of the alane species formed. Here, hydrogen adatoms are restricted to the surface and are not allowed to react with one another to form molecular hydrogen, since it leads to a product that desorbs instantaneously. Furthermore, hydrogen adatoms are assumed to not interact with each other.

Figure 5.3 quantifies the distribution of Al, H, AlH, AlH_2, and AlH_3 for various temperature and initial hydrogen coverages. These simulations show that the distribution of alanes is minimally affected by temperature, but strongly dependent on the amount of hydrogen available. As expected, hydrogen is the limiting reagent, and if it is present, it reacts to completion with Al adatoms to form AlH_3 at all temperatures.

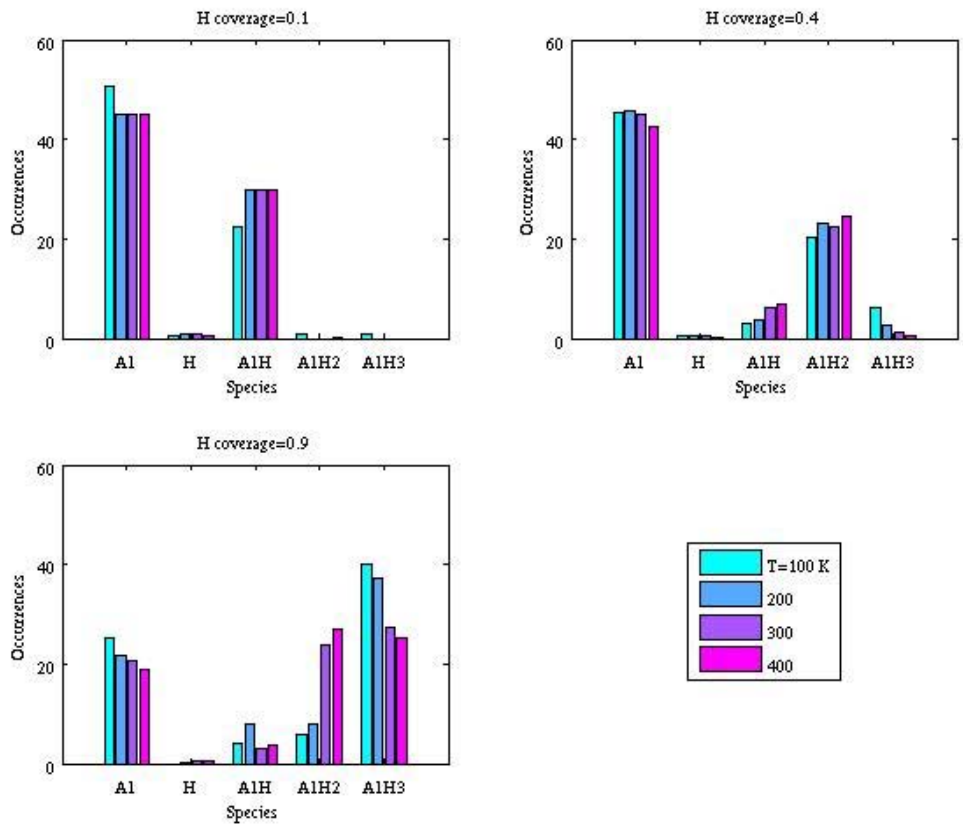

Figure 5.3. Effects of temperature and initial hydrogen coverage on distribution of surface species at equilibrium. The temperature produces only minor qualitative differences, whereas the hydrogen coverage is the limiting factor of the reaction of Al all the way to AlH_3.

In addition to the purely numerical distribution, it is also instructive to consider the spatial distribution of the new surface species. In this two-dimensional model, the hydrogen atoms are not allowed to extract surface aluminum atoms from below as proposed by Go et al. [7], thus limiting the reactions to take place mainly at the step edge. As such, the complete reaction of Al to AlH_3 is only potentially limited by diffusion of AlH_3 away from the step to allow for additional aluminum adatoms to be exposed to the hydrogen. However, the results indicate that this does not prohibit the reactions, and all of the pre-adsorbed hydrogen is able to react, up to the 90% coverage considered. This simple 2D surface model agrees with experiments in that even at low temperatures, the final distribution of surface species is dominated by AlH_3 if there is a sufficient amount of adsorbed hydrogen. The evolution of the surface after the reaction with the adsorbed hydrogen is shown in Figure 5.4. For this simulation, all species have been constrained to remain at step edges because no desorption was allowed, but this constraint will be relaxed in the following section.

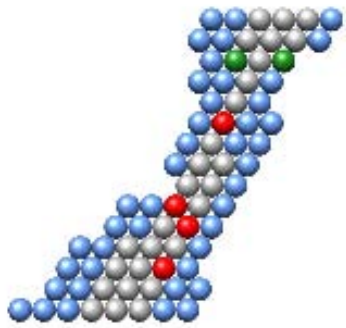

Figure 5.4. Equilibrium state of the surface after reaction with adsorbed hydrogen at 100 K. No desorption was allowed, thus all hydrogen reacted with aluminum, forming AlH_3 (blue) and leaving only a few AlH (red) and AlH_2 (green) molecules remaining with original the aluminum adatoms (gray). Although the step edge has changed shape, using the simple lattice gas model, all species remain at step edges.

5.3. Desorption of Alanes and Step Etching

Although the model is able to predict the surface coverage of alanes, it has not yet captured two important aspects: (1) diffusion of alanes away from the step, and (2) desorption of alanes from the surface. Therefore, in order to produce the step etching seen in experiments, adsorption and desorption are added to the current model. Inclusion of the vapor phase of atomic hydrogen allows not only for adsorption of hydrogen, but also additional reaction pathways which produce H_2 (g). As per experiments, the surface is exposed to a vapor of atomic hydrogen at a relatively low temperature of 180 K where desorption is minimal. In this case, there is an excess of hydrogen, and the surface reaches a dynamic equilibrium consisting of aluminum hydrides only when all of the aluminum adatoms have reacted, as shown in Figure 5.5. At this temperature, there is no desorption of alanes for a binding energy of 0.1 eV. Although this is not technically an equilibrium state as there are still unreacted Al adatoms, it is illustrative of the formation of alanes at the step edges.

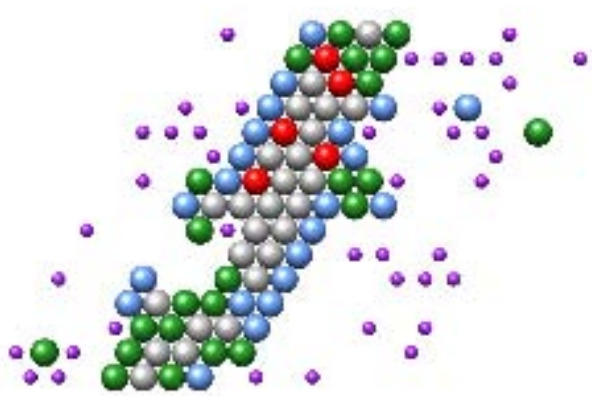

Figure 5.5. Surface after 15,000 time steps at 180 K to adsorb hydrogen onto the surface.

It should be noted that DFT data in the literature indicates preferential binding of hydrogen to step edge sites, but this has not been included in the model. It would have a negligible qualitative effect, and the inclusion of this detail would unnecessarily convolute the analysis. Furthermore, preferential binding of hydrogen would qualitatively enhance the formation of alanes at steps, but the model already sufficiently demonstrates the formation of alanes without this additional consideration.

Next, as done in experiments, the adsorbed sample is heated to room temperature and the surface species begin to desorb. Experiments show desorption of AlH_x reaches a maximum at 340 K. To model this, we place our adsorbed sample directly at 340 K and allow the surface to evolve. While AlH_3 (E_{bind} = 0.99 eV) is more weakly bound to the surface than Al and AlH (E_{bind} ~ 3 eV), this is still too strongly bound to desorb at 340 K as seen in experiments. According to simulations where the binding energy was varied, in order for desorption to occur at 340 K the binding energy must be ~ 0.1 eV, which is much lower than the binding energy at the step edge.

This finding is consistent with the theory AlH_3 in a physisorbed state, as proposed in the mechanism by Chaudhuri et al. [12]. Assuming this binding energy, we find desorption and step-etching of the Al (111) surface at 340 K, as shown in Figure 5.6, in agreement with experiments. However, the mechanism by which chemisorbed AlH_3 at a step edge might be converted to a physisorbed state on the terrace remains unknown. Consequently, the simulations were performed under the assumption that AlH_3 at the step edge may directly desorb to the vapor phase.

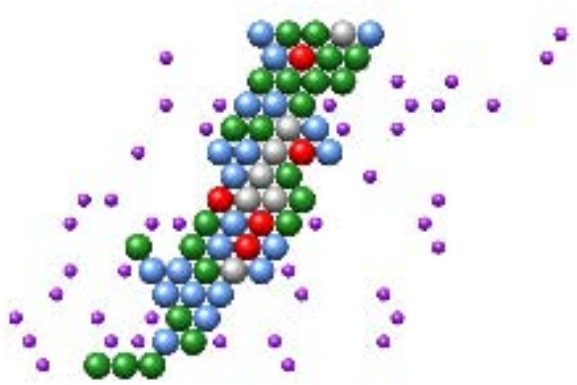

Figure 5.6. Surface structure after placing adsorbed surface Figure 5.5 at 340 K for an additional 15,000 time steps, with desorption energy of AlH_3 specified to be 0.1 eV. The step width is noticeably smaller as AlH_3 has desorbed, effectively etching the step.

6. CONCLUSIONS AND FUTURE WORK

The experimental results show the evolution of the near surface morphology of aluminum when implanted with hydrogen. Small bubbles are initially formed that will eventually coalesce to make larger bubbles and blisters as additional hydrogen ions are implanted. Void growth is preferential along grain boundaries and other microstructural defects in the aluminum, and faceting within voids indicates that some crystallographic planes are likely being etched preferentially. The chemical reaction of hydrogen and aluminum appears to play an important role in the reconstruction of the bombarded region of aluminum because helium, a chemically inert species, produces significantly different morphologies from those produced by hydrogen despite the fact that both gases are virtually insoluble in the aluminum matrix.

The helium implantations in aluminum resulted in the smallest pore sizes and small ligaments of aluminum in the resulting morphology. The relatively high concentration of oxygen in the EDS analysis indicated that more new surface area was formed from the helium implantations than from the hydrogen implantation. The helium implantations appear to be a more promising route to the synthesis of nanostructured metals than the hydrogen implantations. However, helium implantations were not initially the main thrust of the project, and a more complete battery of material characterization remains for future work. The cross-sectional imaging will be crucial for determining the depth to which the nanostructures persist below the surface. It is likely that the depth is slightly less than that of the hydrogen implantations since the penetration depth for helium ions in aluminum should be slightly less than that of hydrogen. Future experiments should attempt higher implantation energies of helium to increase the depth of the implantations, and could even include multiple implantation energies over the same sample area.

The computation simulations show that an aluminum surface exposed to atomic hydrogen will undergo atomic rearrangement leading to surface etching, in agreement with experiments. However, the current model is only two-dimensional and thus neglects additional phenomena which need to be considered. First, in addition to step etching, experiments suggest that hydrogen extracts surface aluminum atoms, resulting in pitting [7]. While this is a three-dimensional phenomenon, it is reasonable to extend the step etching mechanism to the formation of pits on the terrace. Adsorbed hydrogen can extract surface atoms to form AlH, which further reacts with surrounding adsorbed hydrogen to form AlH_3. This species adsorbed on the flat surface is likely to have a lower binding energy than AlH_3 adsorbed at the step edge. This may lead to the creation of the physisorbed phase on the terrace which may more readily desorb due to its lower binding energy, leaving behind a vacancy in the surface. If this series of events is allowed to propagate, it is reasonable to believe they could lead to the formation of pits, which occurs in parallel with the step etching mechanism.

Moreover, the same experiments also show the formation of oligomers on the surface, specifically forming long chains at the original step edges on the surface. While there is little in the literature regarding the formation, DFT calculations have shown Al_2H_6 and Al_3H_9 to be stable surface species [12]. In the current model, migration from a step and transitioning from a chemisorbed state to a physisorbed state are not understood or accounted for. Allowing for the formation of oligomers at the step could easily result in the formation of long chains along the length of the edge, provided its kinetics are favorable, or at least comparable to migration away

from the step. However, it seems that oligomerization and migration from the step would be in competition with each other, so it is uncertain how both can happen simultaneously.

In the context of ion implantation, these surface results provide interesting results. It is evident that the formation of aluminum hydrides is a dominant force behind the mass transfer in the H-Al system. However the details of these reactions are not fully understood on a surface, much less within the bulk. Implanted hydrogen is known to diffuse through the lattice and aggregate to form bubbles. These bubbles are at extremely high pressures surrounded effectively by an Al surface. Due to the extreme pressures within the bubbles, the surrounding Al is subject to an immense flux of hydrogen, orders of magnitude greater than in surface adsorption experiments. This excess of hydrogen is likely to exaggerate the formation of alanes and exaggerate their mass transfer consequences as compared to the simple surface. It is apparent further work needs to be done in understanding the effects of subsurface and bulk hydrogen in aluminum to develop an adequate model to simulate the development of porous nanostructures.

Lastly, exposure of aluminum surfaces to atomic hydrogen is not only a surface phenomenon, but is also thought to result in H atoms occupying subsurface sites, especially at high fluences. A subsurface layer of hydrogen would undeniably alter the thermodynamic energies from DFT calculations, and thus the surface kinetics. It is possible this could explain both the extraction of surface atoms, and more importantly the binding environment and energy of surface clusters. Future modeling of the electronic bonding environment may clarify if there are significant changes to the binding energy due to the presence of hydrogen or other aluminum hydride species. The presence of excess hydrogen could lead to additional repulsive interactions between subsurface H and surface species, facilitation of both the surface mass transfer of aluminum to alanes and their subsequent desorption, and possibly provide a mechanism by which clusters at a step may be forced to the flat terrace in a physisorbed state.

7. REFERENCES

1. Baldwin, M.J. and R.P. Doerner, *Helium induced nanoscopic morphology on tungsten under fusion relevant plasma conditions.* Nuclear Fusion, 2008. **48**(3): p. 5.
2. Chernikov, V.N., et al. *Gas-induced swelling of beryllium implanted with deuterium ions*. in *7th International Conference on Fusion Reactor Materials (ICFRM-7)*. 1995. Obninsk, Russia: Elsevier Science Bv.
3. Doyle, B.L. and D.K. Brice, *Steady state hydrogen transport in solids.* Radiation Effects, 1985. **89**(1-2): p. 21-28.
4. Kamada, K., *Hydrogen Implantation Effects in the Subsurface Layer of Aluminum - Bubble Pressure and Surface Modifications.* Journal of Nuclear Materials, 1989. **169**: p. 141-150.
5. Kamada, K., et al., *Evaluation of Implanted Hydrogen Pressure in Bubbles.* Scripta Metallurgica, 1988. **22**(8): p. 1281-1284.
6. Crane, E.L. and R.G. Nuzzo, *Collision-induced desorption and reaction on hydrogen-covered Al(111) single crystals: Hydrogen in aluminum?* Journal of Physical Chemistry B, 2001. **105**(15): p. 3052-3061.
7. Go, E.P., K. Thuermer, and J.E. Reutt-Robey, *H adsorption and the formation of alane oligomers on Al(111).* Surface Science, 1999. **437**(3): p. 377-385.
8. Condon, J.B. and T. Schober, *Hydrogen Bubbles in Metals.* Journal of Nuclear Materials, 1993. **207**: p. 1-24.
9. Wilson, K.L. and G.J. Thomas, *Low-Energy Helium Implantation of Aluminum.* Journal of Nuclear Materials, 1976. **63**(1): p. 266-272.
10. Hara, M., et al., *Desorption of Aluminum-Hydride from Hydrogen Adsorbed Al(111) Surface.* Journal of Physical Chemistry, 1991. **95**(1): p. 6-7.
11. Winkler, A., C. Resch, and K.D. Rendulic, *Aluminum-Hydride Desorption from Hydrogen Covered Aluminum Single-Crystal Surfaces.* Journal of Chemical Physics, 1991. **95**(10): p. 7682-7688.
12. Chaudhuri, S., et al., *Formation and bonding of alane clusters on Al(111) surfaces studied by infrared absorption spectroscopy and theoretical modeling.* Journal of the American Chemical Society, 2008. **130**(32): p. 10576-10587.
13. Nakajima, T., M. Nakatomi, and K. Yamashita, *Quantum chemical calculations on Al-CVD using DMEAA: surface reaction mechanism of AlH3 on Al(111).* Molecular Physics, 2003. **101**(1-2): p. 267-276.
14. Voter, A.F., *Introduction to the Kinetic Monte Carlo Method*, in *Radiation Effects in Solids*, K.E. Sickafus and E.A. Kotomin, Editors. 2005, Springer, NATO Publishing Unit: Dordrecht, The Netherlands.
15. Kang, H.C. and W.H. Weinberg, *Dynamic Monte-Carlo Simulations of Surface-Rate Processes.* Accounts of Chemical Research, 1992. **25**(6): p. 253-259.
16. Stumpf, R. and M. Scheffler, *Ab initio calculations of energies and self-diffusion on flat and stepped surfaces of Al and their implications on crystal growth.* Physical Review B, 1996. **53**(8): p. 4958-4973.

DISTRIBUTION

1 Ryan DePuit
941 Palermo Drive
Santa Barbara, CA 93105

1	MS1056	Bruce McWatters	1111
1	MS9291	Markus Ong	8651
1	MS9402	Nancy Yang	8651
1	MS9404	Rion Causey	8651
2	MS9018	Central Technical Files	8944
2	MS0899	Technical Library	4536
1	MS0123	D. Chavez, LDRD Office	1011

Sandia National Laboratories